Journal of Materials Chemistry C

Accepted Manuscript

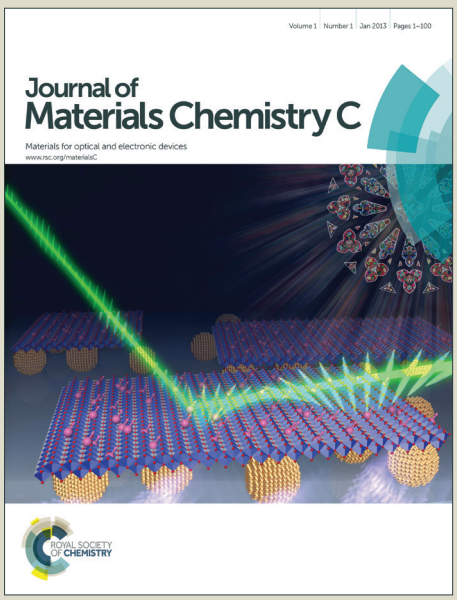

ROYAL SOCIETY OF CHEMISTRY

www.rsc.org/materialsC

Tunable ferromagnetic behavior in Cr doped ZnO nanorod arrays through defect engineering

C.G. Jin,[a] Y. Yang,[a] Z.F. Wu,[d] L.J. Zhuge,[b] Q. Han,[*a] X.M. Wu,[*a] Y.Y. Li,[c] and Z.C. Feng[e]

[a] *Department of Physics, Soochow University, Suzhou 215006, China*

[b] *Analysis and Testing Center, Soochow University, Suzhou 215123, China*

[c] *Institute of Functional Nano and Soft Materials, Soochow University, Suzhou 215123, China*

[d] *Yancheng Institute of Technology, Yancheng 224003, China*

[e] *Institute of Photonics and Optoelectronics, Department of Electrical Engineering, and Center for Emerging Material and Advanced Devices, National Taiwan University, Taipei 106-17, Taiwan*

Abstract

Zn vacancies (V_{Zn}) effects on microstructure and ferromagnetism (FM) properties of $Zn_{0.94}Cr_{0.06}O$ nanorod arrays have been investigated using a combination of experimental measurements and first-principles calculations. The well-aligned $Zn_{0.94}Cr_{0.06}O$ nanorod arrays were synthesized by radio frequency magnetron sputtering deposition at different substrate temperatures. The Cr K-edge X-ray absorption near-edge structure (XANES) and X-ray photoelectron spectroscopy results revealed that the Cr^{3+} ions were located at the substitutional Zn sites. Moreover, the O K-edge XANES analysis and resonance Raman scattering indicated the existence of numerous V_{Zn}. The stable FM observed at room temperature was an intrinsic property of $Zn_{0.94}Cr_{0.06}O$ nanorod arrays. With increasing substrate temperature, an improved crystallinity along with the increase in V_{Zn} was observed in $Zn_{0.94}Cr_{0.06}O$ nanorod arrays, and an enhancement of magnetic moment in the samples came forth. First-principles calculations revealed that the enhanced

[*)] Corresponding author. Tel.: +86-512-6787-0289; Fax: +86-512-6787-0289.
Electronic mail: hanqin@suda.edu.cn (Q. Han), xmwu@suda.edu.cn (X.M. Wu)

magnetism mainly comes from the unsaturated 2*p* orbitals of the surrounding O atoms, which is caused by the presence of the Zn vacancy. This research represents a novel promising route for tuning the magnetic behavior of nano-dilute magnetic semiconductor systems via V_{Zn} changes.

Introduction

Recent advances in ZnO-based dilute magnetic semiconductors (DMSs) have indicated that electronic control of their spin properties can be used to manipulate magnetic signals[1,2]. An alternate approach is to form DMSs, by substituting magnetic ions onto lattice sites of ZnO.[3] It was suggested that a 100% spin-polarized carrier population might be achieved in appropriate systems.[4] ZnO doped with 3d transitional metals (TM) has attracted intense attention because these materials hold the possibility of DMSs with a Curie temperature (T_C) above room temperature (RT).[5] To date, most previous studies on DMSs have focused on bulk and films. One-dimensional (1D) DMSs nanostructures have received much attention because they could potentially be used as building blocks for fabricating 3D architecture of novel spintronics microchips.[6] Realization of spintronic devices from the bottom up might be feasible by adopting DMSs nanowires or nanorods.[7] For example, ferromagnetic DMS nanowires and nanorods are reported to have higher T_c and larger magnetic moment as compared to their bulk and film counterparts.[8] As compared to nonaligned ZnO nano-structures, well-aligned ZnO nanorod arrays demonstrate superior device properties.[9]

To interpret the origin of the magnetic properties, a number of magnetic interaction mechanisms have been proposed, including direct superexchange, indirect superexchange, carrier-mediated exchange,[10] and F-center exchange.[11] There is experimental evidence to suggest that point defects such as oxygen vacancy (V_O),[12] zinc vacancy (V_{Zn}),[13] zinc interstitial,[14] and oxygen interstitial,[15] can mediate ferromagnetic coupling.[16] These results suggest that defects may play an important role in the observed magnetic behaviors of these materials. Therefore, how to control and engineer defects becomes a

very interesting and challenging issue. It would be very useful if defects in these materials could be manipulated to improve the properties of DMSs. Theoretical studies have been carried out to investigate the mechanisms of ferromagnetism associated with defects. The results of first-principles calculations indicate that neutral V_O in ZnO is nonmagnetic,[17] but V_{Zn} does lead to magnetism.[18,19] Currently, the microscopic origin of the high-T_c ferromagnetism (FM) in wide-band-gap DMSs is still under debate.[20] The development of such an understanding has emerged as one of the most important challenges in the magnetism of DMSs.[21]

In this paper, we report an approach of realizing RTFM in Cr-doped ZnO nanorod arrays via complementary experimental radio frequency (RF) plasma synthesis and theoretical spin-polarized density functional theory (DFT) calculations. Photoluminescence (PL) and resonance Raman scattering (RRS) were utilized to detect the possible presence of defects such as V_O, V_{Zn} and Zn_i. X-ray absorption near-edge structure (XANES) spectroscopy and first-principles calculations were utilized to investigate the local atomic and electronic structures as well as magnetic interactions in a $Zn_{0.94}Cr_{0.06}O$ nanorod arrays sample with RTFM. The results show that RTFM is observed which is believed to originate from $Zn_{0.94}Cr_{0.06}O$ nanorod arrays instead of any other secondary phase, which indicates that the V_{Zn} plays an important role in the ferromagnetic origin of $Zn_{0.94}Cr_{0.06}O$ nanorod arrays.

Methods

The $Zn_{0.94}Cr_{0.06}O$ nanorod arrays were grown on p-Si (111) substrates using RF magnetron sputtering technique with a composite target of a ceramic polycrystalline ZnO (60 mm in diameter) containing two Cr pieces (2×2 mm^2) on the surface. Before deposition, the substrates were dipped in acetone to remove surface contamination, dried in a flux of N_2, and then placed into the chamber. After vacuum pumping, the sputtering was performed with an Ar pressure of 2.0 Pa in the chamber evacuated to 5×10^{-4} Pa before an Ar gas flow of 20 sccm was introduced through a mass flow controller. Deposition was then conducted at a RF power of 150 W at different temperatures (RT, 300, 500, 650 °C marked as sample C1, C2, C3, C4 respectively), which was monitored using a thermocouple located under the substrate holder. In addition, no extra catalysts or additives appear in this approach.

The morphology was measured by using a field-emission scanning electron microscope (FE SEM) (Hitachi S-4700). The structural qualities of the nanorod arrays were investigated by X-ray diffraction (XRD) using a Rigaku diffractometer with Cu *Kα* radiation, high-resolution transmission electron microscopy (HRTEM) using a FEI Tecnai G-20 and J.Y. (Jobin Yvon) HR800 Raman system (under excitation of 325 nm at RT). In addition, the chemical state of Cr in the samples was analyzed by KRATOS Analytical X-ray photoelectron spectroscopy (XPS) system. The XANES measurements were performed on beamline 20A in the National Synchrotron Radiation Research Center. Magnetic measurements were performed using a quantum design superconducting quantum interference device (SQUID) magnetometer with the magnetic field parallel to the sample surface. Electrical resistivity measurements were carried out using the

four-point probe system with 1 mA current. All experimental results shown in this paper are for samples $Zn_{0.94}Cr_{0.06}O$ whose compositions were checked by energy dispersive spectroscopy. All the measurements were conducted at RT.

Our spin-polarized DFT calculations are performed by using a 48-atom $Zn_{23}Cr_1O_{24}$ nanorod model; in such a supercell, the Cr concentration is close to the experimental value. We adopted the projected augmented wave (PAW)[22] pseudopotential to describe the core electrons and the general gradient approximation (GGA) of Perdew, Burke, and Ernzerhof (PBE)[23] to account for the exchange and correlation. The kinetic energy cutoff is 400 eV, and the Brillouin zone is sampled by 1×1×3 k-points using the Monkhorst-Pack method. All calculations were implemented by the Cambridge Sequential Total Energy Package (CASTEP).[24]

Results and discussion

The XRD patterns of pure ZnO and the samples C1-C4 are shown in Fig. 1. All peak positions of the samples correspond to the standard diffraction pattern of wurtzite hexagonal ZnO. No other peaks corresponding to either Cr metal or Cr-related oxide phase can be observed within the detection limit of XRD. Also visible in the inset of Fig. 1 is the relative small shift of the (002) peaks for the $Zn_{0.94}Cr_{0.06}O$ nanorod arrays. The *d* (002) value of $Zn_{1-x}Cr_xO$ nanorod arrays decreased from 0.2612 nm for x = 0 to 0.2610 nm for x = 0.06 as demonstrated by plotting the (002) diffraction peak values as a function of $\cos2\theta/\sin\theta$ and extrapolating to $\theta = 90°$.[25] The decrease in lattice parameters is due to the smaller ionic radius Cr^{3+} (0.061 nm) substituting for the larger host ion Zn^{2+} (0.074 nm) at its site in ZnO:Cr. Moreover, with increasing substrate temperatures, crystallinity of nanorod arrays has been strongly improved as the intensity of the (002)

peak has significantly increased. In addition, the full-width at half-maximum (FWHM) of peaks is narrowed with increasing substrate temperatures. The average size of the particle (D) can be calculated according to the Scherrer formula:

$$D = 0.9\lambda / L(2\theta)\cos\theta,$$

where λ is the X-ray wavelength (0.15406 nm), L(2θ) is FWHM, and θ is the diffraction angle. The results show an increase of D from 16 to 29.3 nm.

The FE SEM images of sample C4 are shown in Fig. 2(a). Aligned nanorod arrays were found when the sample was grown at a substrate temperature of 650 °C. These Cr-doped ZnO nanorod arrays are aligned perpendicular to the substrate. The length of the synthesized nanorod arrays is approximately 600 nm. In addition, they are in high density and are uniformly distributed over the substrate. Fig. 2(b) shows the low magnification TEM image of sample C4, which appears to be almost consistent with the FE SEM observations. It shows that the diameter of each naorod has little variation from bottom to top and the average diameter is about 65 nm. HRTEM was performed to determine the state of Cr atoms, which could not be detected by XRD. It provides an insight into the detailed atomic structure of Cr-doped ZnO nanorod arrays. The HRTEM image obtained from a single nanorod is shown in Fig. 2(c). There are no detectable traces of Cr-related secondary phases in the overall of the $Zn_{0.94}Cr_{0.06}O$ nanorod. In contrast, the doping Cr is soluble, i.e., homogeneously distributed in ZnO wurtzite structure. The interplanar spacing of 0.26 nm corresponds to the *d* value of (002) plane. The inset in Fig. 2(c) shows the corresponding selected-area electron diffraction (SAED) pattern, confirming that the $Zn_{0.94}Cr_{0.06}O$ nanorod growth direction is along [001], which is in agreement with the XRD result. The nanorods appear to be single crystalline. Both

techniques proved a preferred orientation growth of $Zn_{0.94}Cr_{0.06}O$ nanocrystals along the *c* axis. Our results suggest that the method used in our experiment can be applied to grow large-scale aligned Cr-doped ZnO nanorod arrays.

Fig. 3(a) displays the RT PL spectra and RRS of $Zn_{0.94}Cr_{0.06}O$ nanorod arrays grown at different substrate temperatures. Sample C4 exhibits clear PL band emission while samples C1, C2 and C3 only show multi-phonon RRS, which indicates that the nonradiative centers relating to the Cr dopants (Cr acted as traps to the excited electrons) decrease with increasing substrate temperature up to 650 ^{o}C. Sample C4 exhibits a sharp near-band-edge emission at 3.31 eV and another emission centered at 3.15 eV as shown in the inset of Fig. 3(a). The 3.31 eV emission band is related to a near band edge transition of ZnO, namely, the recombination of the free excitations. The V_O-related emission at around 2.4 eV is absent in all of the samples deposited at all temperatures. The emission shoulder (3.15 eV) may be assigned to a transition from the conduction band to the V_{Zn} level.[26] This peak is dominant, hence, we suggest the existence of a large amount of V_{Zn} in the $Zn_{0.94}Cr_{0.06}O$ nanorod arrays.

RRS is an important tool in the study of basic physical properties of semiconductors including nanostructure materials. Fig. 3(a) shows multi-phonon RRS of samples C1-C4, excited by the 325 nm laser line (3.81 eV). In general, the number of longitudinal optical (LO) phonons in semiconductors varies monotonically with the polaron coupling coefficient. The polaron coefficient is a measure of the strength of the electron-phonon interaction and determines the availability of relaxation paths and transport properties of the excited electrons in a semiconductor. It is evident from Fig. 3(a) that the maximum LO intensity is at 7LO, which coincides with the energy of the PL at 3.31 eV. This

observation is consistent with an outgoing resonant behavior: $E_{laser} - n\hbar\omega_{LO} = E_g$. In our case, we found n=7 and LO energy is 0.071 eV (corresponding to 570 cm^{-1}). Thus, the scattered energy of the 7LO for a laser excitation line 3.81 eV can be expressed as $3.81 - 7 \times 0.071 \approx 3.31eV$, which is equal to the PL energy (as can be seen in the inset of Fig. 3(a)). Therefore the resonance process is coupled to the electronic states corresponding to those responsible for the PL transitions. There are no detectable traces of Cr-related secondary phase LO in the overall of $Zn_{0.94}Cr_{0.06}O$ nanorod arrays.

Fig. 3(a) also shows that the integrated Raman intensity of first LO phonon (1LO) is larger than that of second LO phonon (2LO). This may be due to impurity or defect scatters, which give contributions to the RRS as well. The I_{2LO}/I_{1LO} ratio as a function of substrate temperature reflects the electron-LO phonon coupling originating from the variation of Fröhlich interactions within the material,[27] as plotted in Fig. 3(b). The I_{2LO}/I_{1LO} increases monotonically with substrate temperature, indicating disorder effects as well as other defect scatter effects on the RRS decrease. When the sample grows at high substrate temperature, the grain size increases and the crystallinity of the nanorod arrays is improved. In addition, it is well known that the second-order structures are very sensitive to atomic scale disorder. As a result, the I_{2LO}/I_{1LO} ratio increases due to the better crystallinity at high substrate temperature. The electron-LO phonon coupling will also be greatly enhanced accordingly.

In order to understand the role of O 2*p* states on the electronic structure of $Zn_{0.94}Cr_{0.06}O$ as a function of substrate temperature, XANES experiments at the O K edge were carried out as shown in Fig. 4. This probes the orbital character of the spectral features of the O 2*p* unoccupied states in the conduction band and its hybridization with

different Cr and Zn orbitals. The observed spectral features are assigned as follows: (a) the energy region between 530–539 eV (marked by A1-A2) is mainly attributed to O 2*p* hybridization with highly dispersive Zn 3*d*4*s* /Cr 3*d* states and (b) the region between 539-550 eV (marked by A3-A4) can be assigned to O 2*p*–Zn 4*p*/Cr 4*sp* hybridized states. The pre-edge peak A2 (537.5 eV) evolves with Cr-doping in ZnO and its intensity increases monotonically with substrate temperature, suggesting a strong hybridization of O 2*p* orbitals with Cr 3*d* states. Thus, a significant enhancement of pre-edge spectral features reveals that the effective doping of Cr in a ZnO matrix induces a strong hybridization of *s*-*p*-*d* orbitals. Therefore, it is reasonable to conclude that Cr ions are incorporated in the system and responsible for the change in the electronic structure of this material. The weak shoulder peak A1 in the pre-edge region of the O K-edge XANES indicates that V_{Zn} is present along with Cr_{Zn} in the $Zn_{0.94}Cr_{0.06}O$ nanorod arrays. This is because that V_{Zn} in Cr-doped ZnO is a shallow acceptor.[28]

Fig. 5(a) shows the normalized Cr K-edge absorption spectrum of $Zn_{0.94}Cr_{0.06}O$ grown at different substrate temperatures, in which three representative features, namely, peaks “B1”, “B2,” and “B3” are observed. The pre-edge peak (peak B1) is ascribed to a 1s→3d transition, while the main absorption is due to a 1s→4p one. Wong et al.[29] have shown that the presence of the pre-edge peak is indicative of a tetrahedral environment of the x-ray absorbing transition metals, which coincides well with the fourfold coordination of substitutional Cr atoms in wurtzite ZnO. Its intensity increases with increasing substrate temperatures, implying a strong 1s→3d transition. XPS was further used to investigate the bonding characteristics and oxidation states of Cr in the nanorod arrays. Fig. 5(b) shows that the Cr $2p_{3/2}$ core line of the nanorod arrays grown at 650 °C centered

208 at 577.1 eV based on Gaussian fitting is a characteristic of Cr^{3+} ions.[30] No Cr, Cr_2O_3,
209 CrO_2, and CrO_3 are observed, indicating that Cr dopants do not exist as metal or oxide
210 clusters. It shows that Cr exists only in the oxidized state. Therefore, the substitutional
211 state of Cr dopants in the nanorod arrays is safely concluded.

212 Magnetic measurements on $Zn_{0.94}Cr_{0.06}O$ nanorod arrays grown at different
213 temperatures were performed using a SQUID magnetometer. All the measurements were
214 corrected by removing the substrate effects. Magnetization versus magnetic field (*M-H*)
215 loops for $Zn_{0.94}Cr_{0.06}O$ nanorod arrays measured at RT, are shown in Fig. 6(a). All three
216 loops are found to be hysteretic, indicating FM at RT. The moment per Cr atom increases
217 with increasing substrate temperature. The sample C1 possesses a net moment of 0.76
218 μ_B/Cr. With increasing substrate temperature up to 650 °C, the value of magnetic moment
219 shows a remarkable increase to 1.16 μ_B/Cr. The coercive forces (H_c) of the $Zn_{0.94}Cr_{0.06}O$
220 nanorod arrays grown at RT, 300, 500 and 650 °C are about 104, 42, 53 and 82 Oe,
221 respectively. The high substrate temperature enhanced the magnetic moment of the
222 system to some extent, but it does not change the magnetic properties of the $Zn_{0.94}Cr_{0.06}O$
223 nanorod arrays drastically. In order to distinguish the intrinsic FM from Cr dioxides, the
224 zero-field cooling (ZFC) and field cooling (FC) magnetization curves of sample C4 were
225 measured at an applied magnetic field of 1000 Oe from 5 K to 400 K as shown in Fig.
226 6(b). It can be seen that the ZFC and FC curves are kept separated up to 400 K. This
227 indicates that the T_C is well above 400 K. Among the impurity phases related to Cr:ZnO
228 systems, CrO_2 is the only ferromagnetic phase (T_C ~ 386 K).[31] However, as the obtained
229 T_C of the $Zn_{0.94}Cr_{0.06}O$ nanorod arrays is well above 400 K, the FM is not from the CrO_2
230 cluster. Therefore the Cr-doped ZnO nanorod arrays are expected to be free of

ferromagnetic precipitates and the FM phenomenon observed in our samples is expected to be intrinsic to the Cr-ZnO matrix.

To gain a deep insight into the origin of the RTFM at atomic level, we performed the spin-polarized DFT calculations by using a 48-atom $Zn_{23}Cr_1O_{24}$ nanorod model (Fig. 7(a)); in such a supercell, the Cr concentration is close to the experimental value. The total magnetic moment is as high as 3.33 μ_B, for the calculated supercell. The obtained densities of states (DOS) are shown in Fig. 8. We found that the magnetism mainly comes from the 3d electrons of Cr ions with the local spin moment of ~3.26 μ_B, and both Zn and O atoms have nearly zero spin contribution (see Fig. 8(a)). The influence of point defects on the magnetism of the Cr-doped ZnO nanorod arrays was also investigated. We considered Zn vacancies and found that V_{Zn} can enhance the magnetism by about 0.7 μ_B as compared with the defect-free system. The spin density and the projection of DOS onto the O 2*p* and Cr 3*d* orbitals are shown in Fig. 8(b); we can see that, besides the magnetic moment induced by Cr atoms, the Zn vacancy also contributes about 0.7 μ_B per V_{Zn} to the total magnetic moment of this system. This enhanced magnetism mainly comes from the unsaturated 2p orbitals of the surrounding O atoms (Fig. 7(b)), which is caused by the presence of the Zn vacancy. These magnetic moments induced by Zn vacancies are aligned by the external magnetic field and further contribute to the total magnetic moment of the system.

The origin of FM in DMS materials remains a very controversial topic. In order to address the origin of FM in $Zn_{0.94}Cr_{0.06}O$ nanorod arrays, electrical resistance of the samples was measured. The resistivity of undoped ZnO is about 0.2-0.3 **Ω** cm but 10^4 **Ω** cm for the $Zn_{0.94}Cr_{0.06}O$ nanorod arrays. The presence of Cr ions in ZnO increases the

resistivity by four orders. This seems to argue against a free carrier mediated mechanism (such as the Ruderman-Kittel-Kasuya-Yoshida-type model).[32] Besides, conventional superexchange interactions can not produce long-range magnetic order at concentrations of magnetic cations of a few percent, i.e., (6 at. %) Cr doped ZnO.[12,33] Some recent studies have shown that the native defects in the ZnO host can induce the RTFM in TM-doped ZnO.[34] Based on the above analysis, we propose that the bound magnetic polarons (BMP) model may be legitimate in our samples. Within the BMP model the long range FM ordering could be formed by either direct overlaps between BMP (i.e., the distance between two polarons is smaller than the polaron diameter) or indirect BMP-magnetic impurities-BMP interactions[35] (i.e., the distance between two polarons can be much larger than the polaron diameter). The latter case is apparently more applicable in highly insulating materials, which do not have many carriers but sufficient magnetic impurities. The magnetic impurities whose density is presumably boosted by the Cr doping can still facilitate the FM alignment of BMP. We suspect that the RTFM of $Zn_{0.94}Cr_{0.06}O$ may be connected with the presence of V_{Zn}. The experimental results show that the enhancement of the magnetic moment may be due to the increase of the V_{Zn} mediated *p-d* exchange interaction between O 2*p* and Cr 3*d* orbitals with increasing substrate temperature, which is consistent with the results of RRS and XANES. The strong hybridization between O 2*p* and Cr 3*d* orbitals gives the spontaneous spin polarization. Thus, these convoluted effects of band alteration, polaronic interaction and orbital hybridization must be carefully taken into account in order to reveal the physics in doped wide-band-gap oxides.

Conclusions

In summary, well-aligned $Zn_{0.94}Cr_{0.06}O$ nanorod arrays were synthesized by the RF plasma deposition method. The $Zn_{0.94}Cr_{0.06}O$ nanorod arrays were aligned perpendicular to the Si substrate. The PL and O K-edge XANES analyses indicate the existence of numerous Zn vacancies. No secondary phase in the sample is found within the XANES and HRTEM detection limits. The saturated magnetization is 1.16 μ_B/Cr at 650 °C and decreases with decreasing substrate temperature. The $Zn_{0.94}Cr_{0.06}O$ nanorod arrays exhibit obvious stable RT ferromagnetic ordering, which is believed to originate from V_{Zn} mediate BMP model. From first-principles calculations, we conclude that the V_{Zn} can be controlled to tune the ferromagnetism of the $Zn_{0.94}Cr_{0.06}O$ nanorod arrays.

Acknowledgments

This work is supported by the National Natural Science Foundation of China (No.11175126 11104197 11204266 11375126), the Key University Science Research Project of Jiangsu Province (13KJA140001), the Natural Science Foundation of Jiangsu Province for the Higher Education Institutions (No.11KJB140011), the Qing Lan Project, the Program for Graduates Research & Innovation in University of Jiangsu Province (No.CXZZ11_0085), and NSC 98-2221-E-002-015-MY3 and 98-3114-E-005-002-CC2, and NTU Excellent Research Project (10R80908).

Notes and references

1 H. Ohno, *Science*, 1998, **281**, 951.

2 S. A. Wolf, D. D. Awschalom, R. A. Buhrman, J. M. Daughton, S. V. Molnar and M. L. Roukes, *Science*, 2001, **294**, 1488.

3 J. K. Furdyna, *J Appl Phys*, 1982, **53**, 7637.

4 R. N. Gurzhi, A. N. Kalinenko, A. I. Kopeliovich, A. V. Yanovsky, E. N. Bogachek and U. Landman, *Phys Rev B*, 2003, **68**, 125113.

5 T. Diel, H. Ohno, F. Matsukura, J. Cibert and D. Ferrand, *Science*, 2000, **287**, 1019.

6 Y. Wu, J. Xiang, C. Yang, W. Lu and C. M. Lieber, *Nature*, 2004, **430**, 61.

7 W. B. Jian, Z. Y. Wu, R. T. Huang, F. R. Chen, J. J. Kai, C. Y. Wu, S. J. Chiang, M. D. Lan and J. J. Lin, *Phys Rev B*, 2006, **73**, 233308.

8 D. Vanmaekelbergh and L. K. van Vugt, *Nanoscale*, 2011, **3**, 2783.

9 Y. Jun, Y. Jung and J. Cheon, *J Am Chem Soc,* 2002, **124**, 615.

10 C. Liu, F. Yun and H. Morkoc, *J Mater Sci:Mater Electron*, 2005, **16**, 555.

11 B.K. Roberts, A. B. Pakhomov, V. S. Shutthanandan and K. M. Krishnan, *J Appl Phys*, 2005, **97**, 10D310.

12 C. G. Jin, T. Yu, Y. Yang, Z. F. Wu, L. J. Zhuge, and X. M. Wu, *Materials Chemistry and Physics*, 2013, **139**, 506.

13 Y. M. Hu, S. S. Li and C. H. Chia, *Appl Phys Lett*, 2011, **98**, 052503.

14 J. L. MacManus-Driscoll, N. Khare, Y. Liu, and M. E. Vickers, *Adv. Mater.*, 2007, **19**, 2925.

15 G. Brauer, W. Anwand, W. Skorupa, J. Kuriplach, O. Melikhova, and C. Moisson, *Phys. Rev. B*, 2006, **74**, 045208.

16 J. Huang, L. Zhu, L. Hu, S. Liu, J. Zhang, H. Zhang, X. Yang, L. Sun, D. Li, and Z. Ye, *Nanoscale*, 2012, **4**, 1627.

17 C. H. Patterson, *Phys. Rev. B*, 2006, **74**, 144432.

18 D. Galland and A. Herve, *Phys. Lett. A*, 1970, **33**, 1.

19 Q. Wang, Q. Sun, G. Chen, Y. Kawazoe, and P. Jena, *Phys. Rev. B*, 2008, **77**, 205411.

20 K. Ando, *Science*, 2006, **312**, 1883.

21 J. M. D. Coey, M. Venkatesan, and C. B. Fitzgerald, *Nat Mater*, 2005, **4**, 173.

22 P. E. Blöchl, *Phys Rev B*, 1994, **50**, 17953.

23 J. P. Perdew and Y. Wang, *Phys Rev B*, 1992, **45**, 13244.

24 S. J. Clark, M. D. Segall, C. J. Pickard, P. J. Hasnip, M. J. Probert and K. Refson, *Z. Kristallogr*, 2005, **220**, 567.

25 B.D. Cullity, *Elements of X-ray Diffraction, 2nded*, Addison-Wesley, Massachusetts, 1978.

26 Y. M. Hu, S. S. Li, and C. H. Chia, *Appl. Phys. Lett.*, 2011, **98**, 052503.

27 J. F. Scott, T. C. Damen, W. T. Silfvast, R. C. C. Leite and L. E. Cheesman, *Opt Commun*, 1970, **1**, 397.

28 W. S. Yan, Z. H. Sun, Q. H. Liu, Z. R. Li, T. F. Shi, F. Wang, Z. M. Qi, G. B. Zhang, S. Q. Wei, H. W. Zhang, and Z. Z. Chen, *Appl Phys Lett*, 2007, **91**, 062113.

29 J. Wong, F. W. Lytle, R. P. Messmer and D. H. Maylotte, *Phys Rev B*, 1984, **30**, 5596.

30 Y. M. Hu, S. S. Li, and C. H. Chia, *Appl. Phys. Lett.*, 2011, **98**, 052503.

31 N. H. Hong, A. Ruyter, W. Prellier, and J. Sakai, *Appl. Phys. Lett.,* 2004, **85**, 6212.

32 C. Song, K. W. Geng, F. Zeng, X. B. Wang, Y. X. Shen, F. Pan, Y. N. Xie, T. Liu, H. T. Zhou and Z. Fan, *Phys Rev B*, 2006, **73**, 024405.

33 N. Khara, M. J. Kappers, M, Wei, M. G. Blamire and J. L. MacManus-Dridcoll, *Adv Mater*, 2006, **18**, 1449.

34 D. Karmakar, S. Mandal, R. Kadam, P. Paulose, A. Rajarajan, T. Nath, A. Das, I. Dasgupta, and G. Das, *Phys. Rev. B*, 2007, **75**, 144404.

35 A. Kaminski and S. D. Sarma, *Phys Rev Lett*, 2002, **88**, 247202.

Figure captions

Fig. 1 XRD patterns of the investigated ZnO samples. The inset shows the enlarged region of the (002) diffraction peak.

Fig. 2. (a) FE SEM images and (b) TEM images of $Zn_{0.94}Cr_{0.06}O$ nanorod arrays grown at 650 °C. (c) HRTEM image of an individual $Zn_{0.94}Cr_{0.06}O$ nanorod and its corresponding SAED pattern at the inset.

Fig. 3. (a) PL spectra and RRS of the $Zn_{0.94}Cr_{0.06}O$ grown at RT, 300, 500 and 650 °C with excitation of 325 nm. The inset shows the PL spectra of the $Zn_{0.94}Cr_{0.06}O$ grown at 650 °C. (b) The ratio of I_{2LO}/ I_{1LO} as a function of the substrate temperature.

Fig. 4. O K-edge experimental XANES spectra of the $Zn_{0.94}Cr_{0.06}O$ grown at RT, 300, 500 and 650 ^{o}C.

Fig. 5. (a) Cr K-edge experimental XANES spectra of the $Zn_{0.94}Cr_{0.06}O$ grown at RT, 300, 500 and 650 °C. (b) XPS spectra showing Cr 2p core level of $Zn_{0.94}Cr_{0.06}O$ nanorod arrays gown at 650 °C.

Fig. 6. (a) *M* vs *H* of $Zn_{0.94}Cr_{0.06}O$ nanorod arrays (grown at RT, 300, 500 and 650 °C, respectively) at RT. (b) ZFC/FC curves for sample C4 measured at 1000 Oe.

Fig. 7. Spin-density isosurface for the $Zn_{23}Cr_1O_{24}$ nanorod arrays (cross-sectional view): (a) without a V_{Zn} and (b) with a V_{Zn}. Here, the Zn, O, and Cr atoms are indicated by gray, red, and blue spheres, respectively.

Fig. 8. The total and projected density of states (DOS) of the $Zn_{23}Cr_1O_{24}$ nanorod arrays: (a) without a V_{Zn} and (b) with a V_{Zn}. The green dotted line indicates the Fermi level.

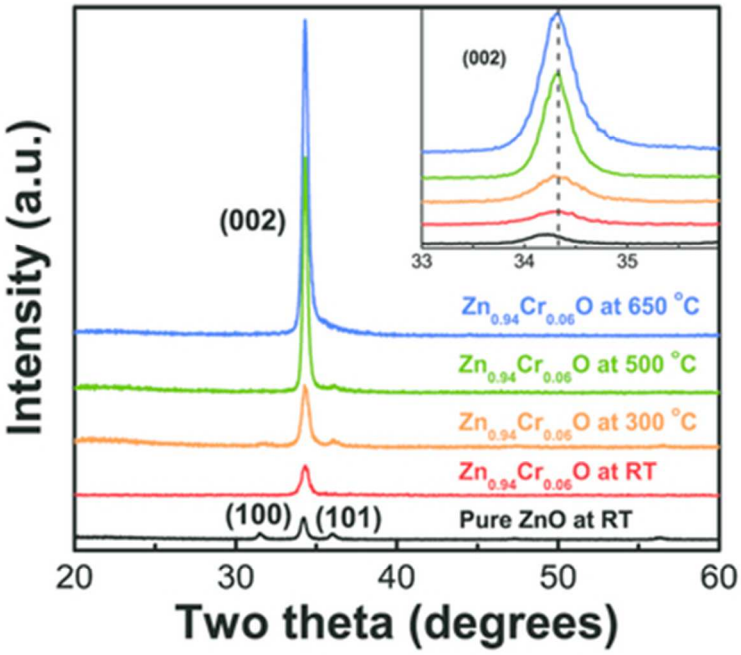

Fig. 1 XRD patterns of the investigated ZnO samples. The inset shows the enlarged region of the (002) diffraction peak.
39x32mm (300 x 300 DPI)

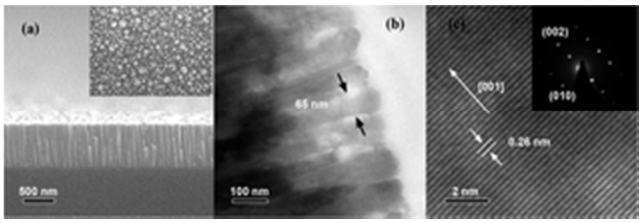

Fig. 2. (a) FE SEM images and (b) TEM images of Zn0.94Cr0.06O nanorod arrays grown at 650 °C. (c) HRTEM image of an individual Zn0.94Cr0.06O nanorod and its corresponding SAED pattern at the inset.
26x8mm (300 x 300 DPI)

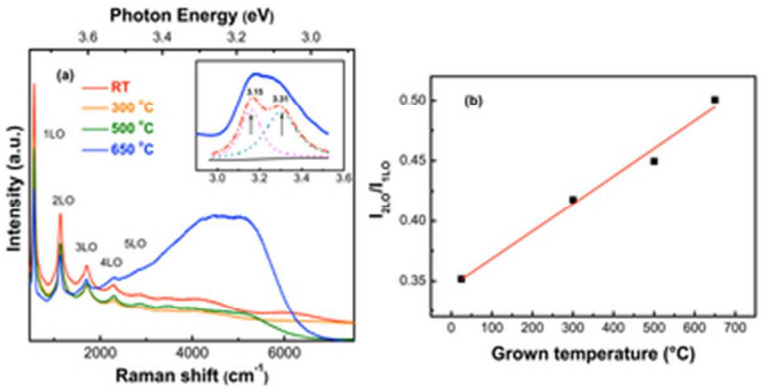

Fig. 3. (a) PL spectra and RRS of the Zn0.94Cr0.06O grown at RT, 300, 500 and 650 °C with excitation of 325 nm. The inset shows the PL spectra of the Zn0.94Cr0.06O grown at 650 °C. (b) The ratio of I2LO/ I1LO as a function of the substrate temperature.
37x17mm (300 x 300 DPI)

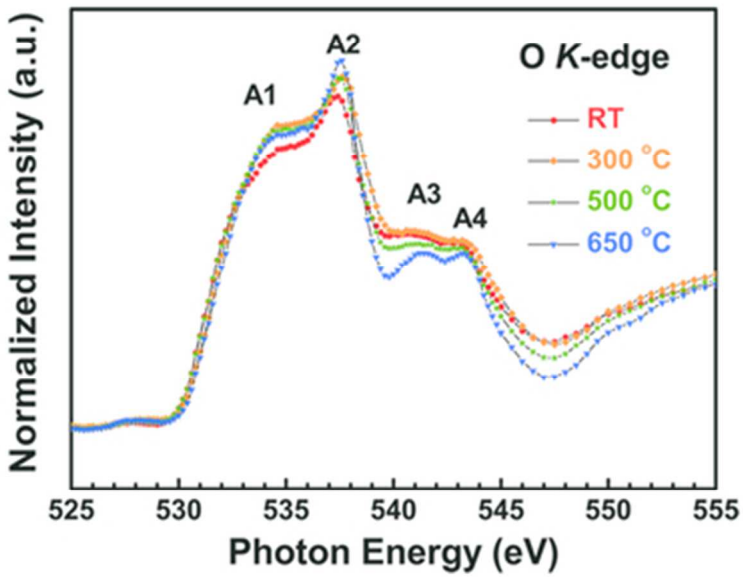

Fig. 4. O K-edge experimental XANES spectra of the Zn0.94Cr0.06O grown at RT, 300, 500 and 650 oC.
39x28mm (300 x 300 DPI)

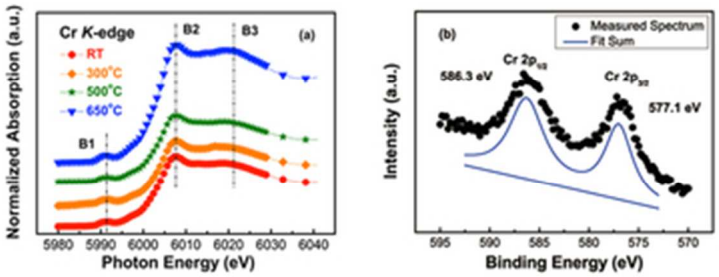

Fig. 5. (a) Cr K-edge experimental XANES spectra of the Zn0.94Cr0.06O grown at RT, 300, 500 and 650 °C. (b) XPS spectra showing Cr 2p core level of Zn0.94Cr0.06O nanorod arrays gown at 650 °C.
32x13mm (300 x 300 DPI)

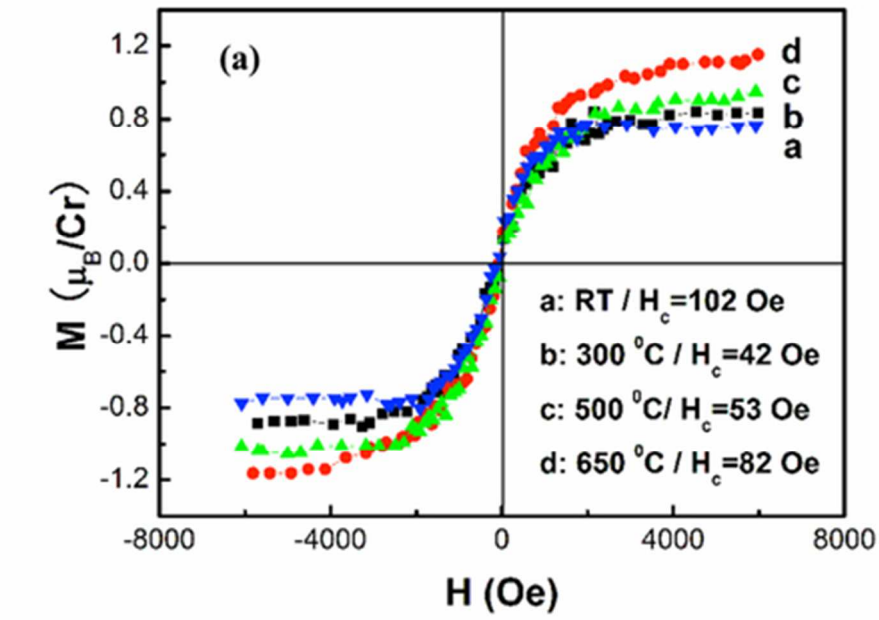

Fig. 6. (a) M vs H of Zn0.94Cr0.06O nanorod arrays (grown at RT, 300, 500 and 650 °C, respectively) at RT.
39x32mm (300 x 300 DPI)

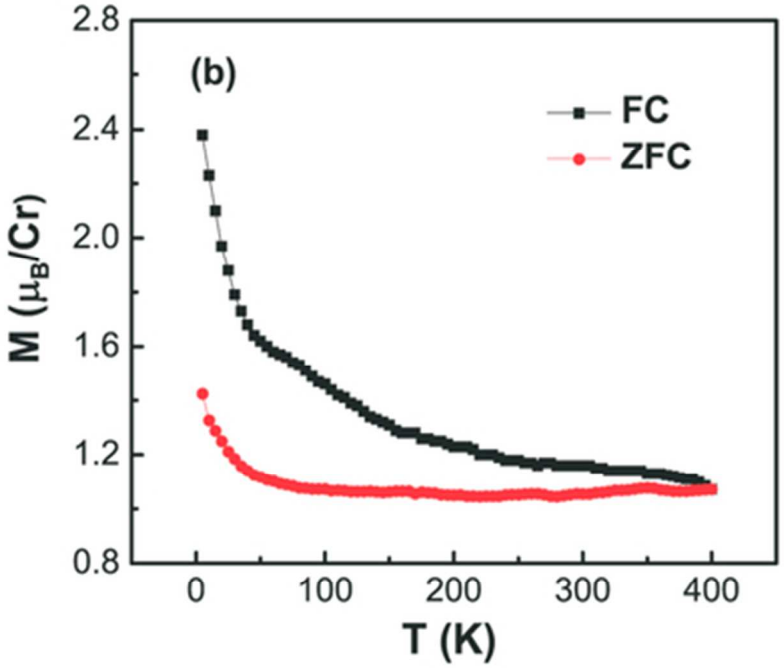

Fig. 6. (b) ZFC/FC curves for sample C4 measured at 1000 Oe.
39x32mm (300 x 300 DPI)

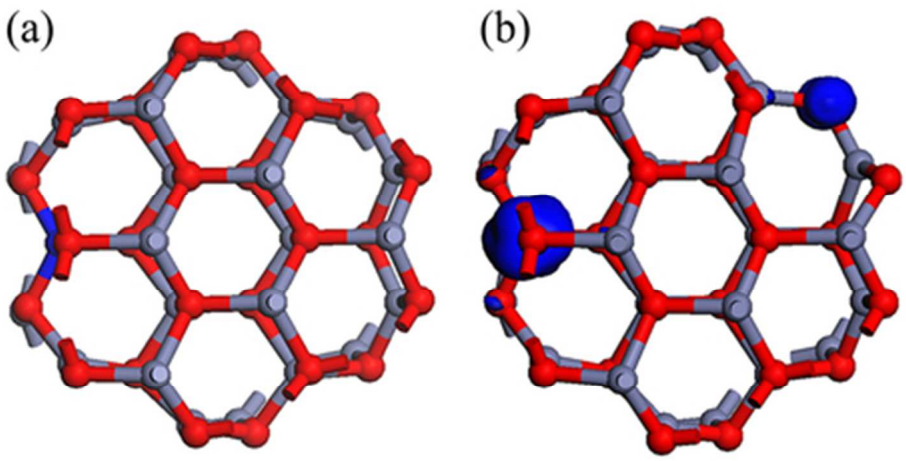

Fig. 7. Spin-density isosurface for the Zn23Cr1O24 nanorod arrays (cross-sectional view): (a) without a VZn and (b) with a VZn. Here, the Zn, O, and Cr atoms are indicated by gray, red, and blue spheres, respectively.
39x20mm (300 x 300 DPI)

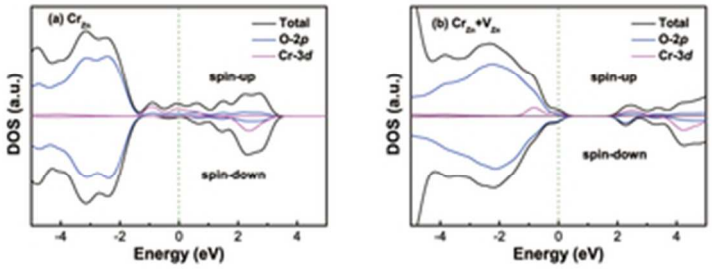

Fig. 8. The total and projected density of states (DOS) of the Zn23Cr1O24 nanorod arrays: (a) without a VZn and (b) with a VZn. The green dotted line indicates the Fermi level.
32x12mm (300 x 300 DPI)